A Resonant Current-Mode Wireless Power Receiver and Battery Charger With −32 dBm Sensitivity for Implantable Systems

Myungjoon Choi, *Student Member, IEEE*, Taekwang Jang, *Student Member, IEEE*, Junwon Jeong, *Student Member, IEEE*, Seokhyeon Jeong, *Student Member, IEEE*, David Blaauw, *Fellow, IEEE*, and Dennis Sylvester, *Fellow, IEEE*

***Abstract*— Wireless power transfer for implantable systems must harvest very low power levels due to low incident power on human tissues and a small receiver coil size. This work proposes resonant current-mode charging to reduce minimum harvestable input power and increase power efficiency at low input power levels. Avoiding rectification and voltage regulation from conventional voltage-mode methods, this work resonates an LC tank for multiple cycles to build up energy, then directly charges a battery with inductor current. A prototype is fabricated in 0.18 μm CMOS technology. Minimum harvestable input power is 600 nW and maximum power efficiency is 67.6% at 4.2 μW input power. Power transmission through bovine tissue is measured to have negligible efficiency loss, making this technique amenable to implantable applications.**

***Index Terms*— Current mode, implantable system, inductor-based harvesting, internet of things, RF harvesting, wireless power transfer.**

I. INTRODUCTION

CONTINUOUS health monitoring has become feasible in part due to miniature implantable sensor systems such as [1]–[4]. Battery recharging capability is essential for such implantable systems because changing a system battery may require surgery, making implantable systems less attractive. For this purpose, wireless power transfer is a popular option because it is non-invasive. However, there are two main challenges. First, strict safety regulations of power exposure on human tissue limit the available incident power at the receiver coil. The specific absorption rate (SAR) limit set by the Federal Communication Commission (FCC) is 4 W/kg, and standards setting organizations typically use 1/10 of this value. In addition to tissue heating issues, non-thermal effects such as altered cell membrane permeability or central nervous system effects can be caused by exposures less than 10 mW/cm^2 [5].

Manuscript received April 29, 2016; revised June 21, 2016; accepted July 28, 2016. Date of publication August 25, 2016; date of current version November 21, 2016. This paper was approved by Guest Editor Edgar Sanchez-Sinencio.

The authors are with the Department of Electrical Engineering and Computer Science, University of Michigan, Ann Arbor, MI 48105 USA (e-mail: myungjun@umich.edu).

Color versions of one or more of the figures in this paper are available online at http://ieeexplore.ieee.org.

Digital Object Identifier 10.1109/JSSC.2016.2598224

Second, implanted systems favor small coils for better biocompatibility and reduced invasiveness. For example, a glucose sensor [2] employs a contact lens form factor with a diameter of 1 cm and a neural recording circuit [3] adopts a receiving power coil with a diameter of 2 cm. The small size of the receiver coil, combined with low incident power, reduces the received power at the coil, making it difficult to obtain sufficient power for implanted devices. This points to the need for high power efficiency transfer techniques, especially at very low received power levels.

As illustrated in Fig. 1, most conventional wireless power receivers are composed of a rectifier for AC-DC conversion, followed by a DC-DC converter or linear regulator to generate an accurate voltage to safely charge a battery. In this voltage-mode approach, the input power (P_{IN}) at the receiver coil must be high enough to overcome the rectifier threshold voltage ($V_{TH,RECT}$), which is set by twice the diode built-in voltage in addition to an input voltage of a DC-DC converter or a linear regulator ($V_{IN,DC-DC}$). Any input power resulting in a voltage less than this cannot be harvested, limiting the minimum harvestable input power ($P_{IN,MIN}$). To address the rectifier threshold voltage issue, transistors with very low threshold voltage can be used as a diode. However, this generally increases the reverse diode current, and often requires additional fabrication steps. Active rectifiers composed of transistors and control circuitry can reduce the diode drop, as used in a previous work [7]. However, the operating frequency of [7] is 13.56 MHz, which is 271.2× faster than this work, requiring a very high bandwidth of the control circuitry to generate accurate switching timing, and thus, consuming substantial power. Even with ideal diodes, the receiver LC tank peak voltage must exceed $V_{IN,DC-DC}$ to harvest. Also, the charging voltage needs to be regulated to ensure battery safety, using a DC-DC converter or a linear regulator, which further reduces power efficiency.

Wireless power receivers can be categorized into two types: coil-based near-field receivers and antenna-based far-field receivers. Coil-based power receivers have relatively high power efficiency, but $P_{IN,MIN}$ ranges from 100s of μW to W [8]–[10]. These systems transmit and receive high power, and thus target high-power applications including

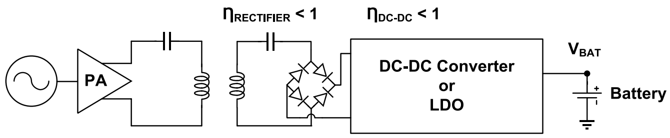

Fig. 1. Block diagram of conventional voltage-mode wireless power transfer system.

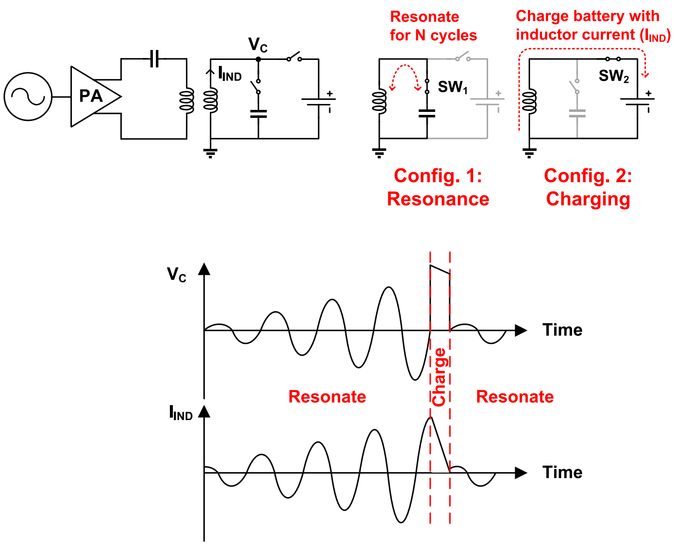

Fig. 2. Block diagram of the proposed resonant current mode wireless power transfer system (top) and its conceptual waveforms at a resonance mode and a charging mode (bottom).

wireless cellular phone charging rather than ultra-low-power implantable device charging. Far-field RF power receivers report lower $P_{IN,MIN}$ of several μW [11], [12], but power efficiency is comparatively low with power efficiency of 15% at 10 μW [13]. Most recently, rectifier-antennas co-design methodology [14-15] achieved sensitivity of -30.7 dBm and -34.5 dBm with a rectifier output voltage of 1 V and 1.6 V, respectively.

This paper is an extension of [16] and introduces a resonant current-mode approach that avoids rectification and voltage regulation. Instead, this method places a capacitor in parallel with a receiver coil to form an LC tank, and then resonates the LC tank for *multiple cycles* to accumulate energy (config. 1). It then transfers this energy to the battery in a boost-converter fashion (config. 2) as shown in Fig. 2. This method has three advantages. First, it improves $P_{IN,MIN}$, as it is no longer limited by $V_{TH,RECT} + V_{IN,DC-DC}$. Second, resonating an LC tank for multiple cycles can optimally balance different types of losses, reducing $P_{IN,MIN}$. In contrast, a non-resonant power receiver [17] employing current-mode charging could not collect power across multiple cycles, which limited its power efficiency at low power levels and resulted in a relatively large $P_{IN,MIN}$ of 7.8 μW. It should be noted that a trade-off exists to implement resonance. The non-resonant receiver [17] does not require an off-chip capacitor for tuning a resonant frequency, and thus, can have a smaller system form factor. Also, power efficiency of [17] is less sensitive to operating frequency variation. Thirdly, because the proposed method directly charges a battery with inductor current, it adopts the advantage of typical current mode charging, which does not require voltage regulation during most of the battery charging phase. Voltage-mode charging demands accurate output voltage to safely charge the battery. Given a process-dependent $V_{TH,RECT}$, a DC-DC converter requires wide input range, wide conversion ratio, and input voltage detection. Removing a voltage regulation eliminates power efficiency loss derived at this step. However, at the final phase of battery charging, typically constant voltage method is preferred as it guarantees safe and accurate full charging. To fully exploit these advantages, a maximum efficiency tracker is designed to optimize key parameters including the number of resonant cycles (N_{RESO}), bias current of a zero crossing detector (I_{BIAS}), and frequency of a V_{BAT} detector (F_{DET}) across a range of input power.

This paper is organized as follows. Section II describes the operating principles of the resonant current-mode wireless power receiver and battery charger, and analytically compares $P_{IN,MIN}$ of the proposed method with that of conventional voltage-mode charging approaches. Section III describes circuit implementations of each block. Section IV analyzes different types of energy losses and power efficiency, and Section V describes the measurement results. Finally, Section VI concludes the paper.

II. Resonant Current-Mode Charging

A. Operating Principles

A simplified diagram and conceptual waveforms of the proposed wireless power transfer system are shown in Fig. 2. A wireless power transmitter, described in the left side, is composed of a sinusoidal signal generator, a power amplifier, an inductor, and a capacitor. A power amplifier amplifies a sine wave generated by the signal generator, and the amplified signal drives the LC tank. On the right side, the proposed wireless power receiver and battery charger are shown. The receiver part has a receiver coil, a parallel capacitor, two switches, a battery, and control circuitry. Resonant frequencies of LC tanks in both sides are tuned to the sine wave frequency of 50 kHz.

This method has two modes: resonance and charging. In a resonance mode, switch 1 is closed and switch 2 is open, and thus, the receiver coil is connected to a parallel capacitor (C_{RX}) and forms an LC tank. As the receiver collects power, V_C amplitude continuously increases across resonant cycles and asymptotically approaches its final value as shown in the bottom of Fig. 2. When V_C is 0 V and rising, all energy in the LC tank is stored in a receiver coil as $E_L = LI_{IND}^2/2$ where I_{IND} is inductor current. A zero crossing detector detects this condition and a digital counter counts the number of resonant cycles. When the count reaches a predetermined value, control circuitry switches the circuit to a charging mode. In this mode, switch 1 is open and switch 2 is closed, which disconnects the receiver coil from C_{RX} and connects it directly to the battery. At this point the energy stored in the inductor charges the battery like a boost converter. As a result, V_C instantly rises to the battery voltage (V_{BAT}) plus $I_{IND} \times R_{SW2}$, and then decreases as E_L is transferred to the battery. R_{SW2}

is the on-resistance of switch 2. Energy transfer is complete when current flowing through switch 2 becomes zero. This condition is sensed by detecting when V_C equals V_{BAT}. When this condition is met, the circuit switches back to resonance mode. The proposed receiver charges a battery by continually repeating this routine.

B. Analysis of Minimum Harvestable Input Power

This subsection compares the minimum harvestable input power ($P_{IN,MIN}$) of the proposed resonant current-mode method and conventional voltage-mode method. The analysis starts by calculating the amplitude of V_C. When V_C is saturated, all energy received per cycle is dissipated in the LC tank at each cycle. The saturated voltage amplitude of V_C ($V_{C,SAT}$) and the saturated current amplitude of I_{IND} ($I_{IND,SAT}$) are given in (1)–(2). Here, Q is the quality factor of the LC tank. T_{Cycle} is one period of the received sine wave.

$$\begin{aligned} E_{Stored\ in\ LC} &= \frac{Q}{2\pi}E_{Loss/cycle} = \frac{Q}{2\pi}E_{Received/cycle} \\ &= \frac{Q}{2\pi}P_{IN}T_{Cycle} = \frac{LP_{IN}}{R_{IND}} = \frac{1}{2}C_{RX}V_{C,SAT}^2 \\ &= \frac{1}{2}LI_{IND,SAT}^2 \end{aligned} \tag{1}$$

$$V_{C,SAT} = \sqrt{\frac{2LP_{IN}}{R_{IND}C_{RX}}}, \quad I_{IND,SAT} = \sqrt{\frac{2P_{IN}}{R_{IND}}} \tag{2}$$

For the conventional rectifier and DC-DC converter structure, as derived in (3)–(4), $P_{IN,MIN}$ is the power such that the resulting V_C equals $V_{TH,RECT}+V_{IN,DC-DC}$ [17]. The lowest $V_{IN,DC-DC}$ found from the literature ranges from 0.12 V to 0.15 V [18-19].

$$V_{C,SAT,MIN} = \sqrt{\frac{2LP_{IN,MIN}}{R_{IND}C_{RX}}} = V_{TH,RECT} + V_{IN,DC-DC} \tag{3}$$

$$P_{IN,MIN} = \frac{R_{IND}C_{RX}(V_{TH,RECT} + V_{IN,DC-DC})^2}{2L}. \tag{4}$$

However, in this proposed current-mode charging, $P_{IN,MIN}$ can be lower than given by (4). If the energy stored in the receiver coil at the end of a resonance mode ($E_{LC,RES}$) can overcome the conduction losses from coil ESR (R_{IND}) and R_{SW2}, the switching loss for mode transitions between a resonance and a charging mode, and the energy overhead of control circuitry, the receiver can harvest power, as described in (5):

$$E_{LC,RES,MIN} = E_{Conduction} + E_{Switching} + E_{control}. \tag{5}$$

To concisely compare two charging methods, we assume that the number of resonant cycle is large enough so that V_C and I_{IND} are saturated in the analysis of (6)–(11). More detailed analysis on the number of resonant cycle is given in Section IV. The circuit in Fig. 3 is used for this analysis. Saturated V_C and I_{IND} in current mode ($V_{C,SAT,CM}$ and $I_{IND,SAT,CM}$, respectively) are smaller than those of a voltage-mode case for the same input power level, since

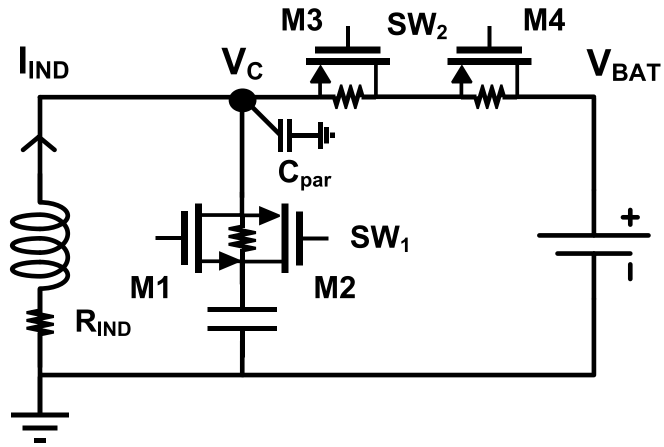

Fig. 3. Schematic of the proposed wireless power receiver with parasitic resistors and capacitors.

on-resistance of the switch 1 (R_{SW1}) adds conduction loss in the LC tank, as derived in (6). As the parasitic resistance of a capacitor (R_{CAP}) is insignificant compared to R_{IND}, R_{CAP} is not included in the analysis.

$$\begin{aligned} V_{C,SAT,CM} &= \sqrt{\frac{2LP_{IN}}{(R_{IND}+R_{SW1})C_{RX}}}, \\ I_{IND,SAT,CM} &= \sqrt{\frac{2P_{IN}}{R_{IND}+R_{SW1}}}. \end{aligned} \tag{6}$$

$E_{Conduction}$ in (5) is the energy I_{IND} dissipates through R_{IND} and R_{SW2} in the charging mode. I_{IND} starts at $I_{IND,SAT,CM}$ and reduces to zero as inductor energy transfers to the battery. Because this charging time (T_{ch}) is very short compared to the resonant period formed by receiver coil inductance and battery capacitance, the inductor current curve can be approximated as linear. As a result, $E_{Conduction}$ can be expressed as (7) below:

$$\begin{aligned} E_{Conduction} &= \int_{t=0}^{Tch} I_{IND}(t)^2 (R_{IND}+R_{SW2})\,dt \\ &= \int_{t=0}^{Tch} \left\{ \sqrt{\frac{2P_{IN}}{R_{IND}+R_{SW1}}} \left(1-\frac{t}{T_{ch}}\right) \right\}^2 \\ &\quad \times (R_{IND}+R_{SW2})\,dt \\ &= \frac{2P_{IN}T_{ch}(R_{IND}+R_{SW2})}{3(R_{IND}+R_{SW1})}. \end{aligned} \tag{7}$$

Equation (5) can be expanded as (8), and solving it gives the minimum harvestable input power in the current-mode charging ($P_{IN,MIN,CM}$) shown in (9). Equation (10) describes switching energy loss for one charging event.

$$\begin{aligned} E_{LC,RES,MIN} &= \frac{LP_{IN,MIN,CM}}{R_{IND}+R_{SW1}} \\ &= \frac{2P_{IN,MIN,CM}T_{ch}(R_{IND}+R_{SW2})}{3(R_{IND}+R_{SW1})} \\ &\quad + \sum C_i V_i^2 + E_{Control} \end{aligned} \tag{8}$$

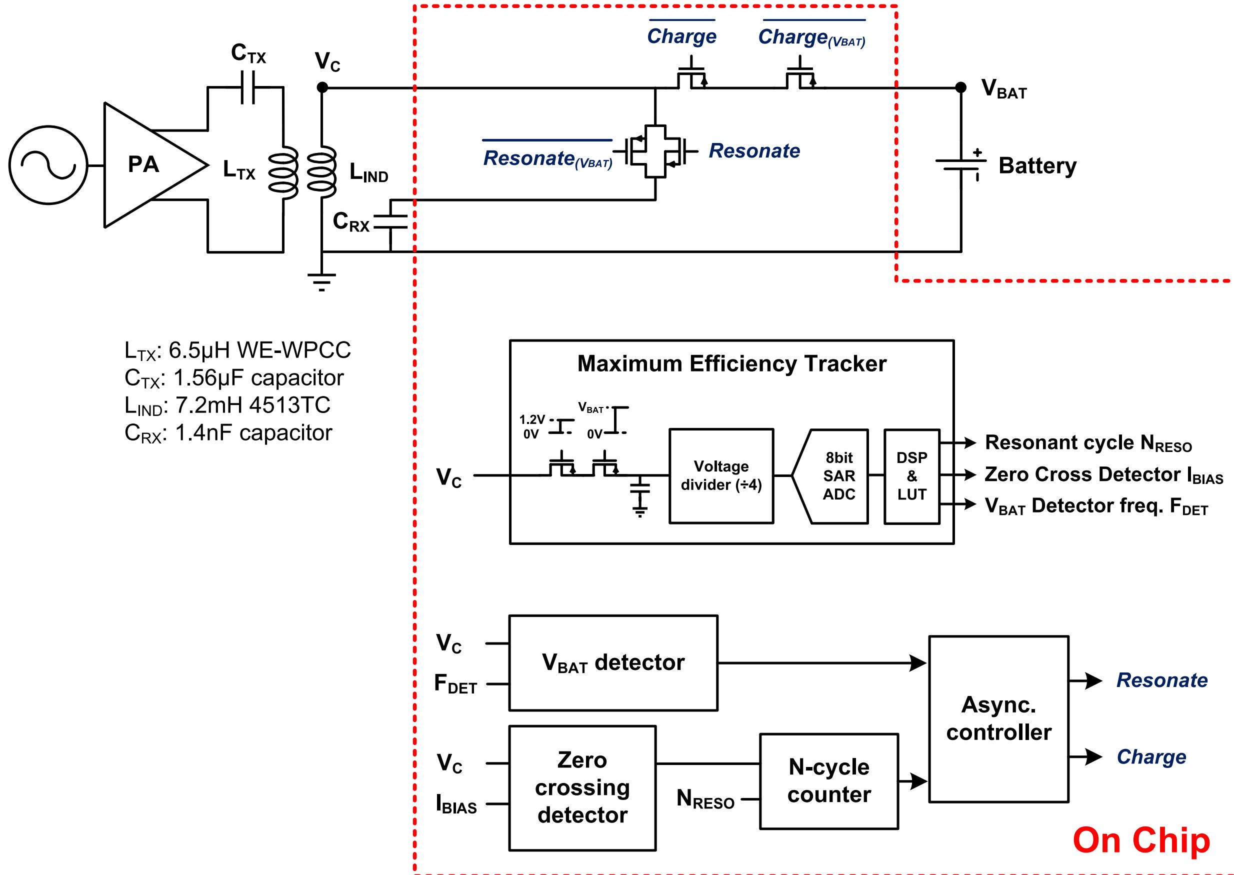

Fig. 4. System diagram of the proposed wireless power transfer system including block diagrams of control circuitry.

$$P_{IN,MIN,CM} = \frac{3\left(\sum C_i V_i^2 + E_{Control}\right)(R_{IND} + R_{SW1})}{3L - 2T_{ch}(R_{IND} + R_{SW2})} \tag{9}$$

$$\begin{aligned} \sum C_i V_i^2 = & \left(C_{G,M1} + C_{G,M3}\right) V_{1.2V}^2 \\ & + \left(C_{G,M2} + C_{G,M4}\right) V_{BAT}^2 \\ & + C_{par}(V_{BAT} + I_{IND} R_{SW2})^2. \end{aligned} \tag{10}$$

From the above equations, the minimum harvestable input power in the proposed approach is clearly no longer related to rectifier threshold voltage and DC-DC converter input voltage. By careful choices of switches and inductor along with low-power control circuit design, this method can overcome the power sensitivity limits of conventional voltage-mode charging.

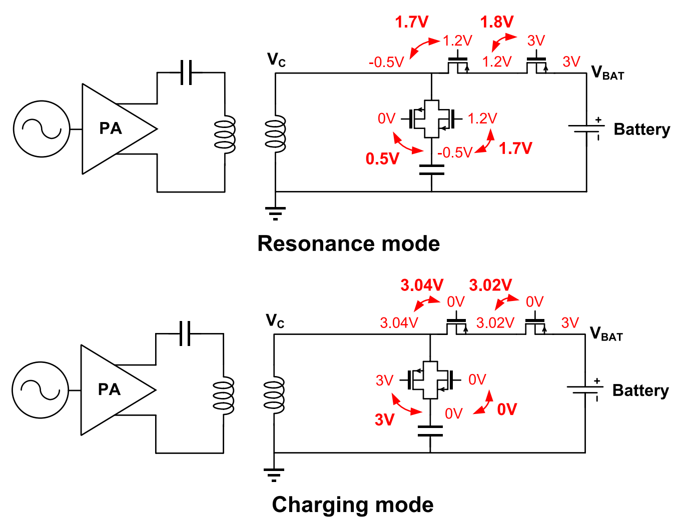

Fig. 5. Proposed receiver at two modes with notation of voltage drops across oxides.

III. Circuit Implementation

A. Power Switches

Fig. 4 shows the proposed system diagram. The power transmitter is drawn on the left side and the proposed power receiver and battery charger is shown at right. All parts inside the red dotted line are integrated on-chip. All four power transistors are 3.3 V I/O devices. Switch 1 in Fig. 2 is implemented with one PMOS transistor and one NMOS transistor connected in parallel. The PMOS transistor and the NMOS transistor are controlled by V_{BAT}-level and 1.2 V-level signals, respectively. Using a 1.2 V signal prevents large source/drain to gate voltages that can cause oxide breakdown when V_C swings to a large negative voltage level during resonance mode. Possible voltages across oxides at resonance mode are shown in Fig. 5. Switch 2 in Fig. 2 consists of two PMOS transistors in series. The left and right PMOS transistors are controlled by 1.2 V and V_{BAT}-level signals, respectively, for the same reason. Oxide voltages in charging mode are also shown in Fig. 5. In this implementation, the

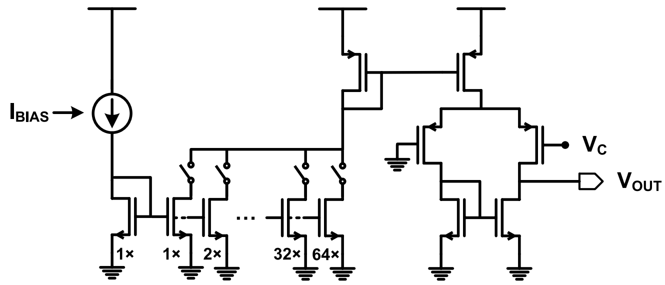

Fig. 6. Schematic of a zero crossing detector.

1.2 V supply is externally provided and power consumption from this source is included in efficiency calculations.

Power transistor sizing should consider the trade-off between switching and conduction losses. As transistor width increases, switching losses increase with higher capacitance while conduction losses decrease with lower on-resistance. Transistor lengths are set to minimum values. Two prototypes of this work are fabricated with different switch sizes. The first version has M1 of 70 μm/350 nm, M2 of 140 μm/300 nm, and M3/M4 are both 35 μm/300 nm. The second version increases M1–M4 widths by 2× compared to the first version. Switching losses are constant across different input power while conduction losses increase with input power. As a result reducing switch sizes lowers $P_{IN,MIN}$ and increasing switch sizes enhances efficiency at high P_{IN}. Measured results are introduced in Section V to support these expected trends.

B. Zero Crossing Detector

After the LC tank builds up enough energy to harvest, the circuit should switch from resonance mode to charging mode. This transition should take place when the inductor stores all the LC tank energy and the parallel capacitor has no energy, and thus V_C is zero. A zero crossing detector detects this condition. It is implemented with a standard one-stage amplifier with differential inputs and a single-ended output as shown in Fig. 6. The two inputs are connected to ground and V_C. PMOS transistors are used as input pairs as the amplifier needs to operate near 0 V. Bias current (I_{BIAS}) is programmable from 3 nA to 200 nA by a maximum efficiency tracker, and the current mirror multiplies the current by 10×.

Limited bandwidth of the zero crossing detector results in a switching voltage error, V_{err}. As a result, C_{RX} has a remaining energy of $C_{RX}V_{err}^2/2$ rather than the ideal 0 J at the end of resonance mode. This energy stored in C_{RX} is wasted by charge redistribution in charging mode and conduction loss in the next resonance mode. Increasing I_{BIAS} reduces this loss by improving zero crossing detector bandwidth, but increases its power consumption. V_{err} is derived in (11), assuming that V_{err} and t_{err} are small. Here α_1 is the ratio of V_C amplitude at ith resonant cycle ($V_{C,cycle,i}$) to V_C amplitude at saturation ($V_{C,peak}$), as shown in (11). The input wave frequency is f_{IN}. Because increasing I_{BIAS} also directly increases amplifier bandwidth, t_{err} can be expressed as in (12). To maintain constant V_{err} and energy loss caused by V_{err} with increasing $V_{C,peak}, I_{BIAS}$ should increase linearly as well. A maximum efficiency tracker therefore measures $V_{C,peak}$ and sets I_{BIAS} accordingly.

$$V_{err} = \alpha_1 V_{C,peak} \sin(2\pi f_{IN} t_{err}) \approx \alpha_1 V_{C,peak} \times 2\pi f_{IN} t_{err} = \frac{2\pi \alpha_1 V_{C,peak} f_{IN}}{\alpha_2 I_{BIAS}} \tag{11}$$

$$\alpha_1 = \frac{V_{C,cycle,i}}{V_{C,peak}}, \frac{1}{t_{err}} = \alpha_2 I_{BIAS}. \tag{12}$$

C. $V_{\mathbf{BAT}}$ Detector

In charging mode, I_{IND} flows through Switch 2 creating a voltage drop of $I_{IND} \times R_{SW2}$ across the switch. A V_{BAT} detector detects when the voltage drop decreases to zero, as the energy transfer is complete at that point. The detector is a dynamic comparator based on [20], as shown in Fig. 7. Its inputs are connected to V_{BAT} and V_C, and the comparator outputs are captured by an SR latch. A clock signal for the comparator is provided by an internal current-starved ring oscillator, of which the frequency is controlled by the maximum efficiency tracker. Charging time is defined as (13) and this time is approximated by the maximum efficiency tracker as follows. L and C_{RX} are fixed, and the peak voltage of V_C at resonance mode ($V_{C,peak}$) is detected with a maximum efficiency tracker. V_{BAT} does not change widely as battery operating voltages are fixed in certain ranges such as 2.25 V to 3 V [21] or 0.9 V to 1.6 V [22] for commercial lithium batteries. With estimation of charging time, V_{BAT} detector is turned on with some delay after the energy transfer starts, in order to reduce power consumption. The delay can be set by a counter and a clock gating NAND gate as in Fig. 7.

$$T_{ch} = \frac{L I_{IND,peak}}{V_{BAT}} = \frac{L\sqrt{C_{RX}V_{C,peak}^2/L}}{V_{BAT}} = \frac{V_{C,peak}\sqrt{C_{RX}L}}{V_{BAT}} = \frac{\alpha_3}{F_{DET}}. \tag{13}$$

A mistimed transition from charging mode to resonance mode leads to energy loss. When the mode is switched too early, inductor energy is not completely transferred to the battery. When the mode is switched too late, all inductor energy is transferred to the battery after which the battery begins discharge to the inductor. From (13), in order to maintain a relative timing resolution (α_3) of detector clock period to T_{ch}, a higher detector frequency (F_{DET}) is required at lower $V_{C,peak}$. A maximum efficiency tracker sets F_{DET} with $V_{C,peak}$ information to keep α_3 constant.

D. Asynchronous Controller

Transitions between the two modes are controlled by event-driven asynchronous logic to eliminate dynamic power during a given configuration. If implemented with synchronous logic, the clock speed is set by the fastest detection speed among trigger events, which is T_{ch}. This timeframe can be shorter than 1 μs at low input power; to detect this transition with precise timing resolution (i.e., 1%), the controller clock frequency must be 100 MHz, consuming several μW and making sub-μW harvesting impossible.

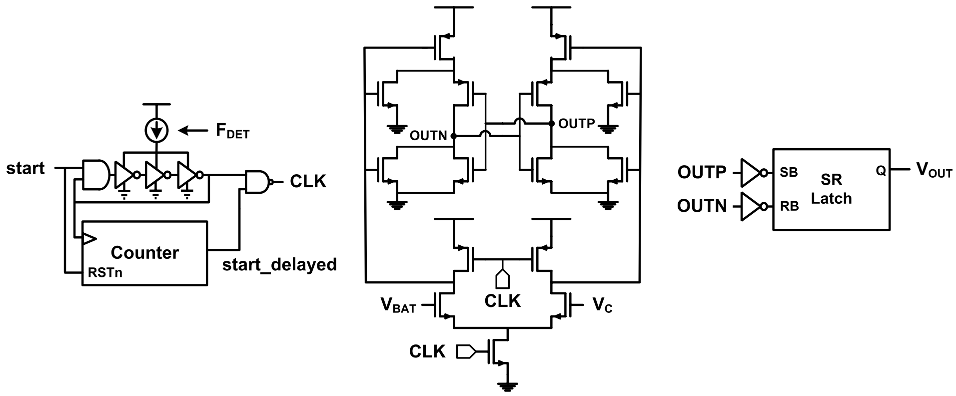

Fig. 7. Schematic of a V_{BAT} detector with its clock generator at left.

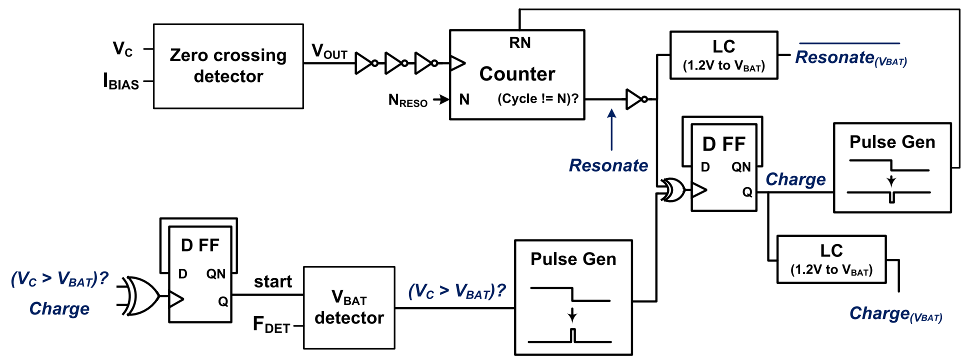

Fig. 8. Block diagram of an asynchronous controller.

Fig. 8 describes the asynchronous controller. The zero crossing detector converts the sinusoidal V_C into a rectangular signal, which serves as the clock for the following counter. The counter outputs a *Resonate* signal when the number of received rising edges reaches a predetermined value, N_{RESO}. N_{RESO} is provided by the maximum efficiency tracker. Level converters generate V_{BAT}-level signals from 1.2 V-level signals. V_{BAT} detector outputs a logic 1 when V_C exceeds V_{BAT}. Pulse generators provide clock inputs to flip-flops as no external clock is available.

E. Maximum Efficiency Tracker

The proposed wireless power receiver and battery charger has three programmable system parameters that can maximize power efficiency across varying input power levels. Input power can vary when the transmitter power changes, or when TX/RX coil separation varies. If the resonant frequency deviates from the operating frequency, input power also changes. In this work, resonant frequency deviation of 100,000 ppm from the operating frequency of 50 kHz decreases the energy stored in C_{RX} at $V_{C,peak}$ by more than 4×. Although dynamically retuning the resonant frequency can recover input power most directly, it requires additional capacitor array. Maximizing efficiency at a given input power can be an alternative solution, as adopted in this work.

The maximum efficiency tracker measures an input power level and set values for these parameters. During initial operation, the system stays in resonance mode and the amplitude of V_C increases. When V_C is saturated, its peak voltage is captured by a sample and hold circuit inside the maximum efficiency tracker. To find the phase where V_C is at its peak, an internal ring oscillator with a high frequency runs for one period of V_C, and a counter counts the number of oscillator cycles. When the count is at half of the number of oscillator cycles, V_C peaks. The sampled V_C peak voltage is then digitized with a standard 8-bit SAR ADC, and a simple on-chip signal processing block and look-up table sets the three parameters to maximize power efficiency: N_{RESO}, I_{BIAS}, and F_{DET}. From (11) and (13), I_{BIAS} is proportional to $V_{C,peak}$, and F_{DET} is inversely proportional to $V_{C,peak}$, so they can be easily calculated. N_{RESO} decreases with increasing $V_{C,peak}$, but the relationship is more complex and is analyzed in Section IV. The SAR ADC operates only once before the charging operation to detect input power level, and is then power gated. Power consumption of the SAR ADC, a power gating controller, and a clock generator is 13.7 μW from simulation. It takes 0.85 μs for one analog to digital conversion, and consumes 11.67 pJ. When power gated, the block consumes 46.8 pW.

IV. Efficiency Analysis

This section analyzes the four kinds of energy losses present in this system: conduction losses and switching losses in each of the resonance and charging modes. The impact of the number of resonant cycles on power efficiency is also analyzed. First, conduction loss in resonance mode ($E_{L,CON,RES}$) is defined as the energy dissipated in R_{IND} and R_{SW1} as derived in (14). $I_{IND,rms,n}$ is a root mean square value of I_{IND} at the n^{th} cycle. N is the number of cycles in resonance mode.

$$E_{L,CON,RES} = \sum_{i=1}^{N} I_{IND,rms,n}^{2} \left(R_{IND} + R_{SW1}\right) T_{Cycle} = \sum_{i=1}^{N} 2\pi\, I_{IND,rms,n}^{2} \left(R_{IND} + R_{SW1}\right)\sqrt{LC_{RX}}. \tag{14}$$

Total energy received during resonance mode is the sum of energy stored in the inductor and the conduction energy loss in the LC tank as derived in (15), as shown at the bottom of this page. Solving this equation for $I_{IND,rms,n}$ gives (16), as shown at the bottom of this page, and substituting this into (14) yields $E_{L,CON,RES}$ in (17), as shown at the bottom of this page. When N is small, this loss term increases rapidly with N with slope approaching $P_{IN}T_{Cycle}$. Also, $E_{L,CON,RES}$ is proportional to P_{IN}.

Second, switching loss when moving from resonance mode to charging mode is $C_{gate,M2}V_{BAT}^{2}$. Here, only the transistors that draw energy from supply voltages are included. This switching loss is independent of N and P_{IN}, as mode switching happens only once per single charging event. Third, conduction loss in charging mode ($E_{L,CON,CH}$) is the energy that I_{IND} dissipates through R_{SW2} and R_{IND}. $I_{IND,N}$ is the peak inductor current at the N^{th} cycle and is $\sqrt{2}\times$ higher than $I_{IND,rms,N}$. $E_{L,CON,CH}$ is derived in (18), which is a generalized version of (7); note that (7) only considers the case when N is large enough such that I_{IND} is saturated. $E_{L,CON,CH}$ increases with N, but also saturates when I_{IND} saturates. It increases with N faster than P_{IN} does, because it is cubically proportional to $I_{IND,N}$ while P_{IN} is proportional to the square of $I_{IND,N}$.

$$\begin{aligned} E_{L,CON,CH} &= \int_{t=0}^{Tch} I_{IND}(t)^{2}\left(R_{SW2}+R_{IND}\right)dt \\ &= \int_{t=0}^{Tch} \left\{ I_{IND,N}\left(1-\frac{t}{T_{ch}}\right)\right\}^{2}\left(R_{SW2}+R_{IND}\right)dt \\ &= \frac{I_{IND,N}^{2}\left(R_{SW2}+R_{IND}\right)}{3}T_{ch} \\ &= \frac{I_{IND,N}^{2}\left(R_{SW2}+R_{IND}\right)LI_{IND,N}}{3V_{BAT}} \\ &= \frac{I_{IND,N}^{3}\left(R_{SW2}+R_{IND}\right)}{3}. \end{aligned} \tag{18}$$

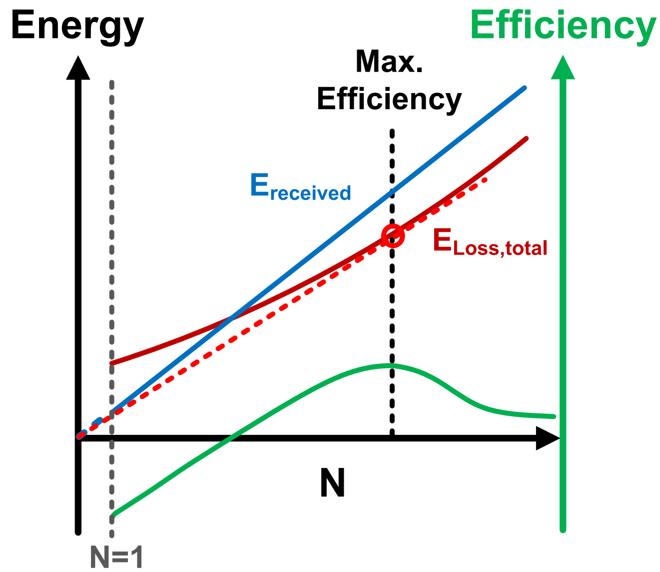

Fig. 9. Conceptual graphs of received energy, total energy loss, and power efficiency with respect to the number of resonant cycles (N).

Finally, switching loss when transitioning from charging mode to resonance mode is $(C_{gate,M1} + C_{gate,M3})V_{DD}^{2} + (C_{gate,M4}+C_{par})V_{BAT}^{2}$. C_{par} is the parasitic capacitance at node V_C in Fig. 3. This loss is independent of N and P_{IN}.

Resonating the LC tank more than 1 cycle during resonance mode improves power efficiency at low input power levels. This is highlighted by the fact that if the energy stored in an LC tank for one resonant cycle is less than the switching losses of Switch 1 and Switch 2, conduction loss of R_{SW1}, R_{SW2} and R_{IND}, and other control overhead, the system cannot charge the battery. However, if the LC tank resonates for additional cycles, the LC tank builds up sufficient energy to overcome these losses, enabling harvesting at the same (small) input power level. However, resonating for too many cycles can decrease power efficiency as $E_{L,CON,RES}$ grows with N at the same rate the LC tank energy does while $E_{L,CON,CH}$ increases with N more rapidly than LC tank energy. At the same time, loss due to charging events per unit time decreases as N increases. In this way, a given input power exhibits a corresponding optimal N that balances the aforementioned losses. Increasing N is more beneficial for low P_{IN}, since at high P_{IN} the large I_{IND} results in high conduction loss, which limits gains from large N. Conceptual waveforms of

$$nP_{IN}T_{Cycle} = \frac{1}{2}L(\sqrt{2}I_{IND,rms,n})^{2} + \sum_{i=1}^{n} 2\pi\, I_{IND,rms,i}^{2}\left(R_{IND}+R_{SW1}\right)\sqrt{LC_{RX}} \tag{15}$$

$$I_{IND,rms,n} = \sqrt{\frac{2\pi\sqrt{LC_{RX}}P_{IN}}{L+2\pi\sqrt{LC_{RX}}\left(R_{IND}+R_{SW1}\right)}\sum_{i=1}^{n}\left\{\frac{L}{L+2\pi\sqrt{LC_{RX}}\left(R_{IND}+R_{SW1}\right)}\right\}^{i-1}} \tag{16}$$

$$E_{L,CON,RES} = \frac{4\pi^{2}\left(R_{IND}+R_{SW1}\right)LC_{RX}P_{IN}}{L+2\pi\sqrt{LC_{RX}}\left(R_{IND}+R_{SW1}\right)}\sum_{n=1}^{N}\sum_{i=1}^{n}\left\{\frac{L}{L+2\pi\sqrt{LC_{RX}}\left(R_{IND}+R_{SW1}\right)}\right\}^{i-1}. \tag{17}$$

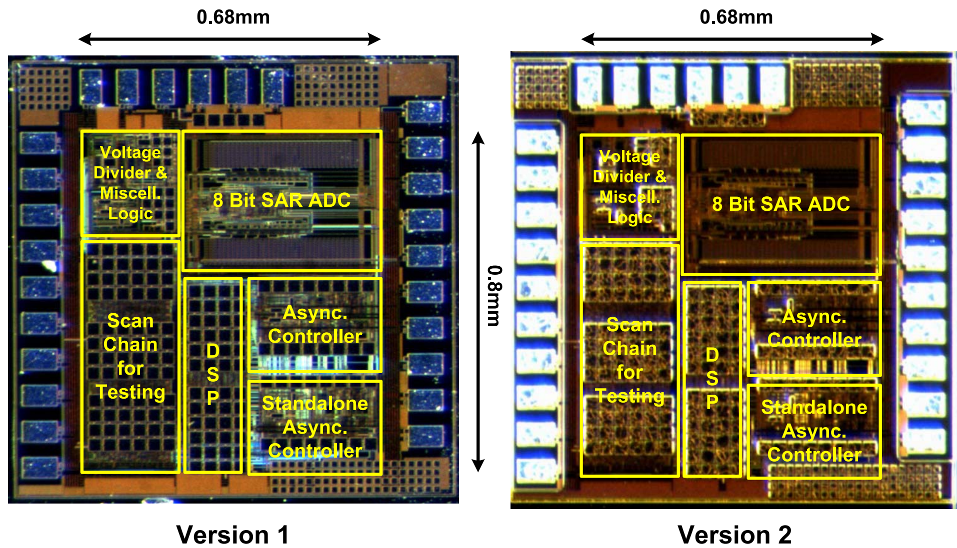

Fig. 10. Microphotograph of two 0.18 μm test chips (0.68 $\times$ 0.8 mm^2 each).

the total energy loss, energy received, and power efficiency with respect to N are plotted in Fig. 9. The N that maximizes power efficiency occurs where a straight line from $N = 0$ touches the loss curve.

V. Measurement Results

Two versions of the proposed work are fabricated in 0.18 μm standard CMOS technology with different sizes of power transistors, as mentioned in Section III. Measurement results of the first version are reported in [16]. The system includes a 7.2 mH Coilcraft 4513TC receiver coil with Q-factor of 51 and 1.4 nF off-chip capacitor. Average on-resistances of the parallel connection of M1 and M2 are 56 Ω for version 1 and 28 Ω for version 2. Parasitic resistance of C_{RX} is negligible. From Fig. 2, config. 1, I_{IND} flows the loop formed by L_{IND} and C_{RX} in series. LC tank's Q-factors of version 1 and 2 are 15.4 and 19.1 from (19), respectively.

$$Q = \frac{1}{R_{IND} + R_{SW1}}\sqrt{\frac{L_{IND}}{C_{RX}}}. \tag{19}$$

The chip area is 0.544 mm^2 for each version, as seen in Fig. 10. The design is composed of an asynchronous controller, a maximum efficiency tracker (consisting of a 8-bit SAR ADC, a digital signal processor, and a voltage divider with miscellaneous logic gates), and a scan chain for testing. A standalone asynchronous controller is added for testing purposes. The receiver coil is 11.7 mm $\times$ 3.5 mm $\times$ 2.6 mm, which is sufficiently small to be implanted in applications such as neural recorders and cochlear implants [3-4].

Fig. 11 shows the testing setup. To minimize parasitic capacitance at the inductor node (C_{par}), chip-on-board packaging is used. A fabricated chip is wirebonded and encapsulated in black epoxy. A WE-WPCC wireless power charging transmitter coil is chosen as a TX coil, and a ceramic off-chip capacitor forms a TX-side LC tank. The TX coil has inductance of 6.5 μH. A board spacer and holder is used to accurately

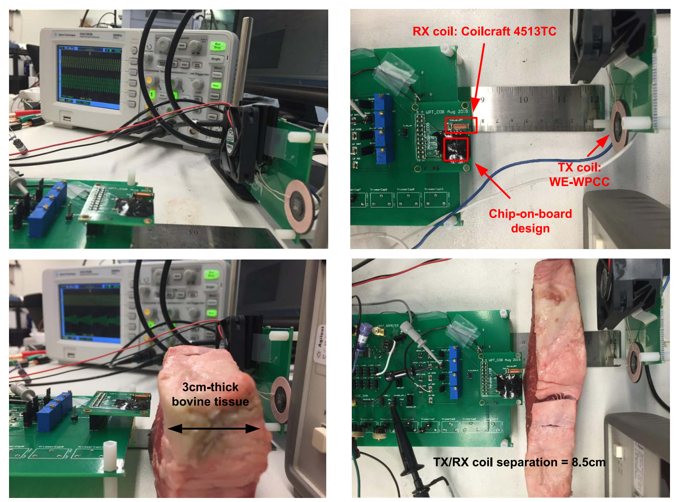

Fig. 11. Measurement setups of the wireless power transfer system.

control TX/RX separation with 1 mm resolution. Because this charging method injects current to a battery for a short time, this current cannot be captured accurately by equipment such as a sourcemeter. Instead, an off-chip capacitor (C_{OUT}) with known capacitance is connected to the output node, and the voltage change (ΔV_{OUT}) over a known time ($t_{measure}$) is measured. An aluminum electrolytic capacitor is used. The capacitor has leakage current I_{Leak}, so this self-discharge rate is measured separately and calibrated out. A battery is also measured to prove charging capability and is shown to be functional. However, because the voltage to charge capacity curve is not linear and varies over recharging cycles, the output power cannot be accurately measured using a battery load. The output power (P_{OUT}) is calculated from (20).

$$P_{OUT} = \int \left(C_{OUT}\frac{\Delta V_{OUT}}{t_{measure}} - I_{Leak} \right) V_{OUT}(t)dt. \tag{20}$$

Measured minimum harvestable input power from version 1 (600 nW) is 3.9$\times$ lower than [9], which exhibited

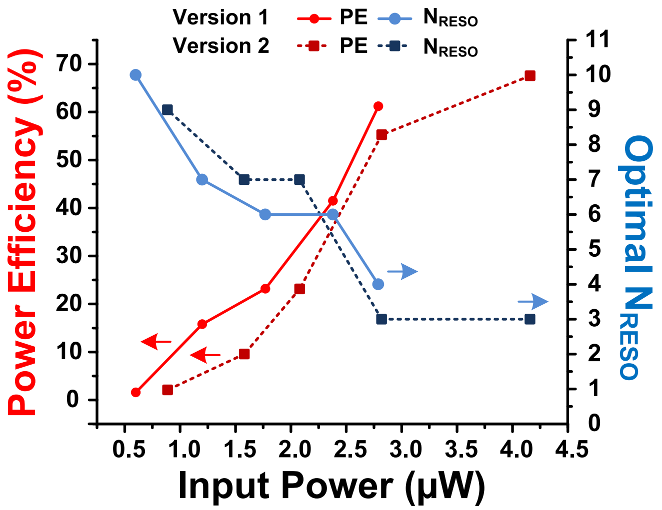

Fig. 12. Measured power efficiencies and optimal N_{RESO} of versions 1 and 2 with respect to input power.

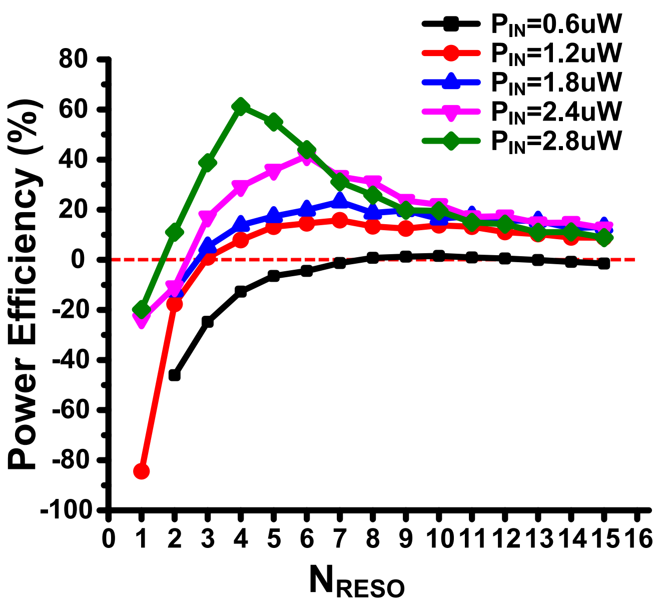

Fig. 13. Measured power efficiency at different input power with respect to N_{RESO} of version 1.

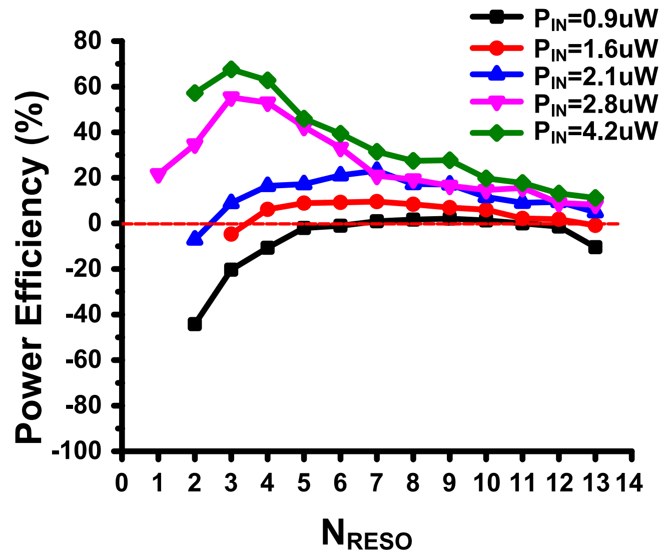

Fig. 14. Measured power efficiency at different input power with respect to N_{RESO} of version 2.

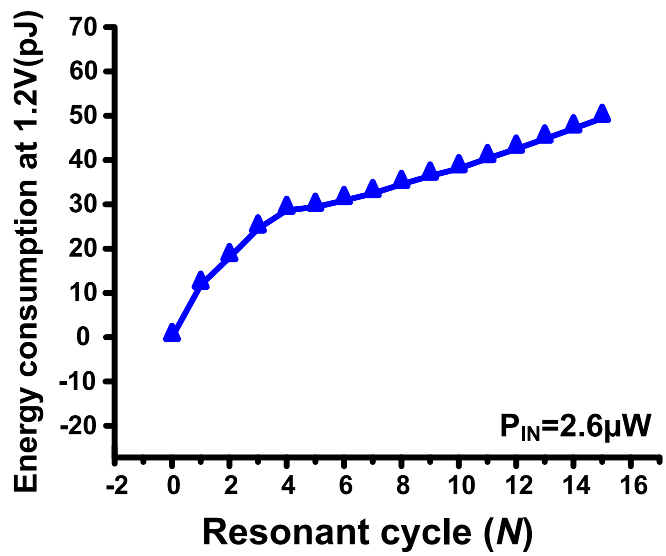

Fig. 15. Measured energy consumption at external 1.2 V supply with respect to N.

the lowest harvestable input power at the time of publication, and 13× lower than [17], which uses the same size coil. A recently published receiver [14] achieves 1.69× lower sensitivity than this work using a self-oscillating technique and a receiver coil with higher Q-factor of 120, but a lower peak efficiency of 27.7%. Version 2 harvests at input power levels above 890 nW. This version's larger switches reduce conduction losses but increase switching losses for mode transitions, and the fixed amount of switching losses has the strongest impact on minimum harvestable input power.

Power efficiency increases as input power increases, reaching 61.2% at $P_{IN} = 2.8\,\mu$W and 67.6% at $P_{IN} = 4.2\,\mu$W for versions 1 and 2, respectively (Fig. 12). In version 1, 600 nW P_{IN} is harvestable when N reaches 7 with optimal N of 10. For version 2, 890 nW P_{IN} becomes harvestable when N exceeds 7 with an optimal N of 9. Optimal N decreases as P_{IN} increases. For version 1, at $P_{IN} = 2.8\,\mu$W, optimal N is 4, and for version 2, at $P_{IN} = 4.2\,\mu$W, optimal N is 3. Figs. 13 and 14 show measured efficiencies at different input power levels with respect to N for version 1 and 2, respectively. The maximum allowable V_C amplitude without device breakdown issues can be found from a resonance mode in Fig. 5. When 1.2 V is used for M1 and M2 gates (3.3 V IO transistor), maximum V_C amplitude is 2.1 V, resulting in the maximum harvestable input power of 46 μW. With a 20 mW transmitter the maximum separation of TX/RX coils is 8.5 cm in air. Identical performance is measured through 3 cm of bovine tissue and 5.5 cm air. This is expected

TABLE I
PERFORMANCE SUMMARY AND COMPARISON

	This Work	[15] RFIC 2015	[11] VLSIC 2013	[12] JSSC 2008	[17] ESTPE 2015	[9] BCAS 2012	[13] MTT 2015	[8] ISSCC 2015	[10] ISSCC 2015
Technology (μm)	0.18	0.065	0.09	0.25	0.18	0.065	Off-chip	0.35	0.13
Chip area(mm^2)	0.544	0.8	0.029	0.4	0.26	0.6	N/A	5.415	14.44
Frequency (MHz)	0.05	2,400	868	906	0.125	1,860	900 / 1,800 / 2,100 / 2,450	13.56	6.78
Min. Harvestable P_{IN} (μW)	0.6	0.85	2.34	5.5	7.8*	200	N/A	N/A	N/A
Max. Receiver Efficiency @ P_{IN}	67.7% @ 4.2μW	38% @ 5μW**	31.5% @ 31.6μW	60% @ 158μW	84% @ 660μW	31.9% @ 500μW	84% @ 3.8mW	92.5% @ 59.45mW	84.6% @ 7.09W
Pickup Coil Size	2.6×3.5×11.7mm^3	1.33 cm^2	20.9cm^2	30cm^2	2.6×3.5×11.7mm^3	2mm×2mm	10cm×10cm	9.5mm diameter	N/A
Coil/ Antenna	Coil	Antenna	Antenna	Antenna	Coil	Antenna	Antenna	Coil	Coil
Measured distance @ TX Power	8.5cm @ 20mW	20m @ 4W	25 m @ 1.78W	15m @ 4W	7cm @ N/A	5cm @ 2W	50m @ 1.2mW/m^2	1.8cm @ 50mW	6mm @ N/A
Charging method	Resonant current-mode	Voltage-mode	Voltage-mode	Voltage-mode	Current-mode	Voltage-mode	Voltage-mode	Voltage-Mode	Voltage-mode
Off-chip components in receivers	L (inductor) , C (capacitor)	L	L	L	L	L	L, C	L	N/A

* Quiescent system power is reported. Min. harvestable P_{IN} is not available.
** Estimated from Figure 4 (c) in [15].

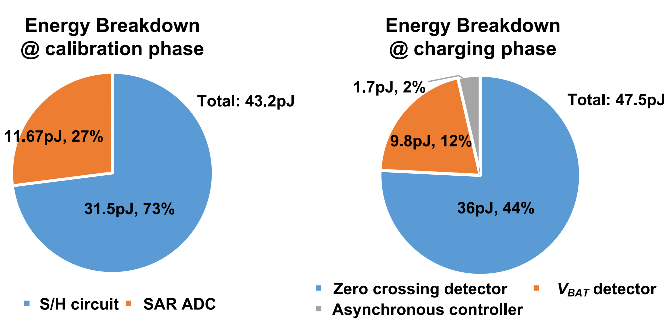

Fig. 16. Energy breakdown at calibration and charging phase for version 2 with $P_{IN} = 4.2$ μW, and $N = 3$ (simulated).

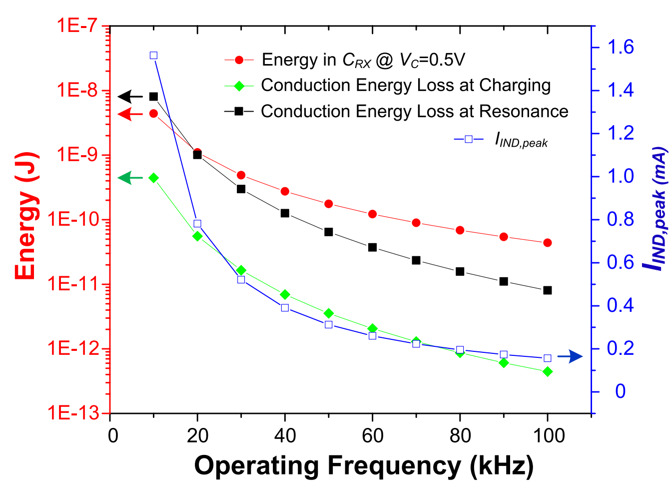

Fig. 17. Stored energy in C_{RX}, energy losses, and $I_{IND,peak}$ with respect to operating frequency (simulated).

since theoretically tissue absorbs negligible power at 50 kHz. According to [23], theoretical power loss, $P = P_0 e^{-2\alpha\sqrt{F}D}$, ($P_0$ = incident power, $\alpha = 2 \times 10^{-3}$ $\sec^{1/2}m^{-1}$ for muscle, $F = 50$ kHz, $D = 3$ cm) is less than 2.7%. This result supports our target application where an implantable system is charged by an external transmitter under the energy exposure limits of human tissue. Energy consumption from the external 1.2 V supply voltage is measured with respect to N at input power of 2.6 μW as shown in Fig. 15. This energy is the energy consumption sum of a zero crossing detector, an asynchronous controller and power transistors M1 and M3. This work

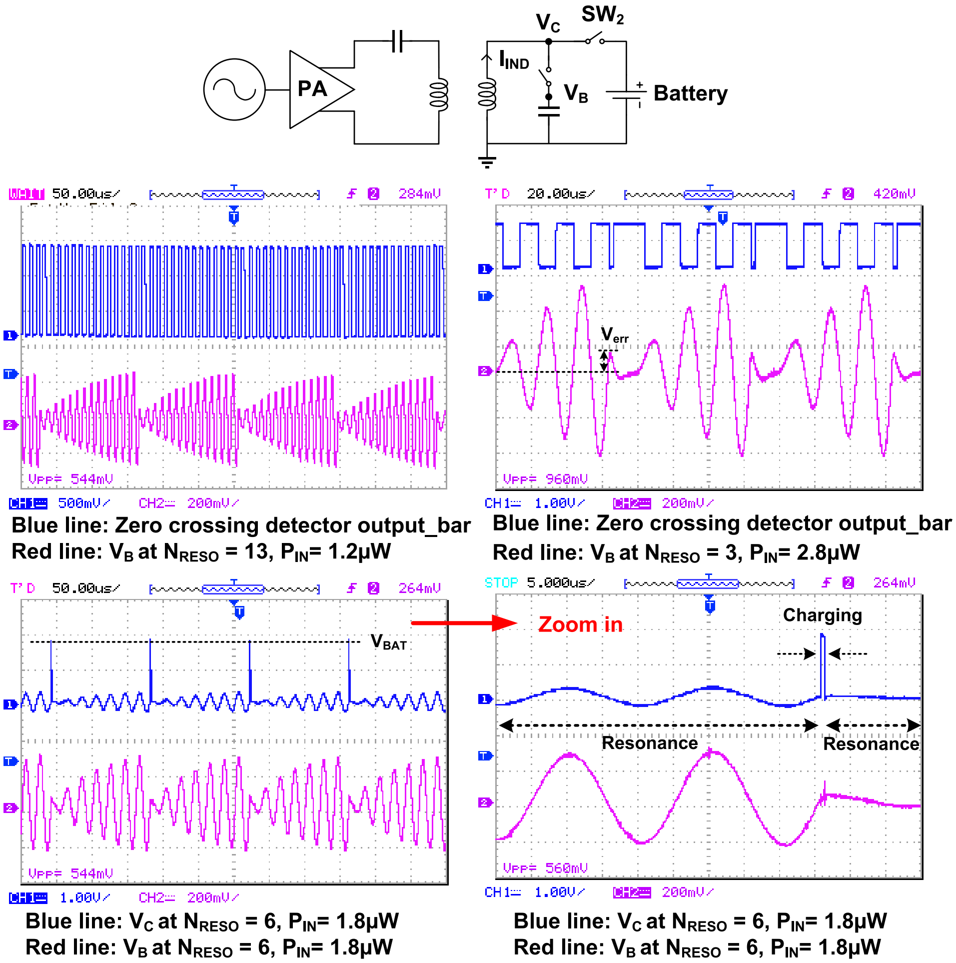

Fig. 18. Measured waveforms of voltages at V_B and V_C, and inverted zero crossing detector output with oscilloscope.

assumes an external 1.2 V source and V_{BAT} to be greater than 1.2 V. These assumptions lower $P_{IN,MIN}$. Some of the previous works [11-13] can start harvesting with no external sources, which can charge overly depleted batteries. Such an assumption runs counter to applications where a cold start is necessary, but for applications where transmitted power is limited, this work can start harvesting from a lower input power.

Energy breakdown of each block is discussed here. The following analysis is for the case of $N = 3$, $P_{IN} = 4.2\ \mu$W for version 2. System operation is divided into two phases: calibration and charging operation. In calibration mode, a maximum efficiency tracker is on and all other blocks do not operate. A sample and hold circuit including an amplifier consumes 31.5 pJ for 0.1 μs and the 8 bit SAR ADC consumes 11.67 pJ for 0.85 μs. After calibration, the maximum efficiency tracker is power gated and the system switches to normal charging operation, where system energy consumption is divided into zero crossing detector energy, V_{BAT} detector energy, and asynchronous controller energy. The sum of all block's energy consumption for one charging event is 47.5 pJ. The zero crossing detector, the V_{BAT} detector, and the asynchronous controller consume 36 pJ, 9.8 pJ, and 1.7 pJ, respectively. Energy breakdowns in these two phases based on simulations are shown as pie charts in Fig. 16.

Increasing operating frequency with a given receiver coil requires reducing C_{RX}. This decreases the energy stored in C_{RX} at the same V_C, I_{IND} amplitude, and thus, amount of conduction energy losses. Meanwhile, switching energy loss per one charging event is fixed for given power switch sizes regardless of the operating frequency. These trends are analyzed in Fig. 17. To concentrate on the effect of operating frequency, a few assumptions are applied for the analysis of Fig. 17: switch sizes are the same as those of version 1 and N is large enough so that I_{IND} is saturated.

Oscilloscope waveforms in Fig. 18 show the zero crossing detector output as blue lines and V_B as red lines. The top left figure shows V_B building up during resonance mode. At top right, V_{err} caused by finite bandwidth of the zero crossing detector is captured. In the bottom left, V_C is measured. In charging mode, V_C rises past V_{BAT} to allow charging and in resonance mode, it tracks V_B. A zoomed-in waveform is captured at bottom right, clearly showing the behavior of V_C in charging and resonance modes.

Table I summarizes the performance of this work and compares to prior art. This work shows a sub-μW minimum harvestable input power and maximum power efficiency of 67.6% at $>$ 7.5$\times$ lower input power than state-of-the-art works. Measured distance between TX/RX coils is 8.5 cm with the lowest TX power of 20 mW among specified TX powers.

VI. Conclusion

This paper proposes a resonant current-mode wireless power receiver and battery charger. The proposed prototype is fabricated in 0.18 μm CMOS technology with area of 0.544 mm^2. Unlike a conventional voltage-mode receiver that rectifies input wave and converts the rectifier output with a DC-DC converter or a linear regulator, this method directly charges a battery with inductor current. Furthermore, the LC tank resonates for multiple cycles to maximize its power efficiency by balancing switching and conduction losses. This work achieves a very low minimum harvestable input power of 600 nW, and maximum efficiency greater than 60% at $> 7.5\times$ lower input power than related work. Power transmission through bovine tissue is demonstrated to validate operation in implantable applications.

References

[1] M. H. Ghaed *et al.*, "Circuits for a cubic-millimeter energy-autonomous wireless intraocular pressure monitor," *IEEE Trans. Circuits Syst. I, Reg. Papers*, vol. 60, no. 12, pp. 3152–3162, Dec. 2013.

[2] Y.-T. Liao, H. Yao, A. Lingley, B. Parviz, and B. P. Otis, "A 3-μW CMOS glucose sensor for wireless contact-lens tear glucose monitoring," *IEEE J. Solid-State Circuits*, vol. 47, no. 1, pp. 335–344, Jan. 2012.

[3] D. A. Borton, M. Yin, J. Aceros, and A. Nurmikko, "An implantable wireless neural interface for recording cortical circuit dynamics in moving primates," *J. Neural Eng.*, vol. 10, no. 2, p. 026010, Feb. 2013.

[4] M. Yip, R. Jin, H. H. Nakajima, K. M. Stankovic, and A. P. Chandrakasan, "A fully-implantable cochlear implant SoC with piezoelectric middle-ear sensor and arbitrary waveform neural stimulation," *IEEE J. Solid-State Circuits*, vol. 50, no. 1, pp. 214–229, Jan. 2015.

[5] J. Leavey, *RF and Microwave Safety Manual*. 2009.

[6] J.-H. Choi, S.-K. Yeo, C.-B. Park, S. Park, J.-S. Lee, and G.-H. Cho, "A resonant regulating rectifier (3R) operating at 6.78 MHz for a 6W wireless charger with 86% efficiency," in *IEEE ISSCC Dig. Tech. Papers*, 2013, pp. 64–65.

[7] Y. Lu, X. Li, W.-H. Ki, C.-Y. Tsui, and C. P. Yue, "A 13.56MHz fully integrated 1X/2X active rectifier with compensated bias current for inductively powered devices," in *IEEE ISSCC Dig. Tech. Papers*, 2013, pp. 66–67.

[8] X. Li, C.-Y. Tsui, and W.-H. Ki, "Wireless power transfer system using primary equalizer for coupling- and load-range extension in bio-implant applications," in *IEEE ISSCC Dig. Tech. Papers*, 2015, pp. 1–3.

[9] D. Pivonka, A. Yakovlev, A. S. Y. Poon, and T. Meng, "A mm-sized wirelessly powered and remotely controlled locomotive implant," *IEEE Trans. Biomed. Circuits Syst.*, vol. 6, no. 6, pp. 523–532, Dec. 2012.

[10] K.-G. Moh *et al.*, "A fully integrated 6W wireless power receiver operating at 6.78MHz with magnetic resonance coupling," in *IEEE ISSCC Dig. Tech. Papers*, 2015, pp. 1–3.

[11] M. Stoopman, S. Keyrouz, H. J. Visser, K. Philips, and W. A. Serdijn, "A self-calibrating RF energy harvester generating 1V at –26.3dBm," in *Proc. IEEE Symp. VLSI Circuits*, Jun. 2013, pp. 226–227.

[12] T. Le, K. Mayaram, and T. Fiez, "Efficient far-field radio frequency energy harvesting for passively powered sensor networks," *IEEE J. Solid-State Circuits*, vol. 43, no. 5, pp. 1287–1302, May 2008.

[13] V. Kuhn *et al.*, "A multi-band stacked RF energy harvester with RF-to-DC efficiency up to 84%," *IEEE Trans. Microw. Theory Techn.*, vol. 63, no. 5, pp. 1768–1778, May 2015.

[14] J. Kang, P. Y. Chiang, and A. Natarajan, "A 1.2cm^2 2.4GHz self-oscillating rectifier-antenna achieving –34.5dBm sensitivity for wirelessly powered sensors," in *IEEE ISSCC Dig. Tech. Papers*, 2016, pp. 374–375.

[15] J. Kang, P. Chiang, and A. Natarajan, "A 3.6cm2 wirelessly-powered UWB SoC with –30.7dBm rectifier sensitivity and sub-10cm range resolution," in *Proc. IEEE Radio Freq. Integr. Circuits Symp. (RFIC)*, May 2015, pp. 255–258.

[16] M. Choi, T. Jang, J. Jeong, S. Jeong, D. Blaauw, and D. Sylvester, "A current-mode wireless power receiver with optimal resonant cycle tracking for implantable systems," in *IEEE ISSCC Dig. Tech. Papers*, 2016, pp. 372–373.

[17] O. Lazaro and G. A. Rincón-Mora, "A nonresonant self-synchronizing inductively coupled 0.18-μm CMOS power receiver and charger," *IEEE J. Emerg. Sel. Topics Power Electron.*, vol. 3, no. 1, pp. 261–271, Mar. 2015.

[18] P.-H. Chen *et al.*, "A 120-mV input, fully integrated dual-mode charge pump in 65-nm CMOS for thermoelectric energy harvester," in *Proc. Asia South Pacific Design Autom. Conf. (ASP-DAC)*, Jan. 2012, pp. 469–470.

[19] J. Kim, P. K. T. Mok, and C. Kim, "A 0.15V-input energy-harvesting charge pump with switching body biasing and adaptive dead-time for efficiency improvement," in *IEEE ISSCC Dig. Tech. Papers*, 2014, pp. 394–395.

[20] M. Miyahara, Y. Asada, D. Paik, and A. Matsuzawa, "A low-noise self-calibrating dynamic comparator for high-speed ADCs," in *Proc. IEEE Asian Solid-State Circuits Conf. (A-SSCC)*, Nov. 2008, pp. 269–272.

[21] Manganese Lithium Coin Batteries (ML Series): Individual Specifications, Panasonic, Osaka, Japan, Aug. 2005.

[22] TS-H Lithium Rechargeable Battery, Seiko Instrument Inc., Chiba, Japan, 2007.

[23] R. A. Freitas, Jr., *Nanomedicine: Basic Capabilities*, vol. 1. Georgetown, TX, USA: Landes Bioscience, 1999.

Myungjoon Choi (S'12) received the B.S. degree (*summa cum laude*) in electrical engineering from the Korea Advanced Institute of Science and Technology (KAIST), Daejeon, South Korea, in 2012, and the M.S. degree in electrical engineering from the University of Michigan, Ann Arbor, MI, USA, in 2014. He is currently working towards the Ph.D. degree at the University of Michigan.

His research interests include fully integrated system clock generation, reference current generation, resistive sensor interface circuits, and wireless power transfer circuits for ultra-low power wireless sensor node.

Mr. Choi is a recipient of the Doctoral Fellowship from Kwanjeong Educational Foundation in Korea.

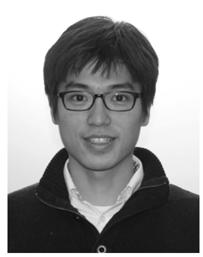

Taekwang Jang (S'13) received the B.S. and M.S. degrees in electrical engineering from Korea Advanced Institute of Science and Technology (KAIST), Daejeon, South Korea, in 2006 and 2008, respectively. In 2008, he joined Samsung Electronics Company Ltd., Giheung, Korea, where he was involved in charge-pump and all digital phase-locked loop design for application processors and digital TV tuners. Since 2013, he has been working toward the Ph.D. degree at the University of Michigan, Ann Arbor, MI, USA.

His research interests include system clock generation, data converters and ultra-low power sensor node design.

Junwon Jeong (S'12) received the B.S. degree in electrical engineering from Korea University, Seoul, Korea, in 2012, where he is currently working toward an integrated M.S. and Ph.D. degree.

His research interests include integrated power management system designs, low-voltage low-power CMOS analog circuit designs, energy harvesting circuit designs and fuel gauging circuit designs.

Seokhyeon Jeong (S'12) received the B.S degree in electrical engineering from the Korea Institute of Science and Technology (KAIST), Daejeon, South Korea, in 2011. He is currently pursuing the Ph.D. degree in electrical engineering at the University of Michigan, Ann Arbor, MI, USA.

His research interests include subthreshold circuit designs, ultra-low power sensors, and the design of millimeter-scale computing systems.

David Blaauw (M'94–SM'07–F'12) received the B.S. degree in physics and computer science from Duke University, Durham, NC, USA, in 1986, and the Ph.D. degree in computer science from the University of Illinois, Urbana, IL, USA, in 1991.

After his studies, he worked for Motorola, Inc. in Austin, TX, USA, where he was the manager of the High Performance Design Technology group. Since August 2001, he has been on the faculty at the University of Michigan, Ann Arbor, MI, USA, where he is a Professor. He has published over 500 papers and holds 50 patents. His work has focused on VLSI design with particular emphasis on ultra-low power and high performance design for ultra-low power sensor nodes.

Prof. Blaauw was the Technical Program Chair and General Chair for the International Symposium on Low Power Electronic and Design (ISLPED). He was also the Technical Program Co-Chair of the ACM/IEEE Design Automation Conference and a member of the ISSCC Technical Program Committee.

Dennis Sylvester (S'95–M'00–SM'04–F'11) received the Ph.D. degree in electrical engineering from the University of California, Berkeley, CA, USA, where his dissertation was recognized with the David J. Sakrison Memorial Prize as the most outstanding research in the UC-Berkeley EECS department.

He is a Professor of electrical engineering and computer science at the University of Michigan, Ann Arbor, MI, USA, and Director of the Michigan Integrated Circuits Laboratory (MICL), a group of ten faculty and 70+ graduate students. He has held research staff positions in the Advanced Technology Group of Synopsys, Mountain View, CA, USA, Hewlett-Packard Laboratories in Palo Alto, CA, USA, and visiting professorships at the National University of Singapore and Nanyang Technological University. He has published over 400 articles along with one book and several book chapters. His research interests include the design of millimeter-scale computing systems and energy efficient near-threshold computing. He holds 29 U.S. patents. He also serves as a consultant and technical advisory board member for electronic design automation and semiconductor firms in these areas. He co-founded Ambiq Micro, a fabless semiconductor company developing ultra-low power mixed-signal solutions for compact wireless devices.

Dr. Sylvester has received an NSF CAREER award, the Beatrice Winner Award at ISSCC, an IBM Faculty Award, an SRC Inventor Recognition Award, and ten best paper awards and nominations. He is a recipient of the ACM SIGDA Outstanding New Faculty Award and the University of Michigan Henry Russel Award for distinguished scholarship. He serves on the technical program committee of the IEEE International Solid-State Circuits Conference and previously served on the executive committee of the ACM/IEEE Design Automation Conference. He has served as an Associate Editor for IEEE TRANSACTIONS ON CAD and IEEE TRANSACTIONS ON VLSI SYSTEMS and a Guest Editor for the IEEE JOURNAL OF SOLID-STATE CIRCUITS and IEEE TRANSACTIONS ON CIRCUITS AND SYSTEMS II.